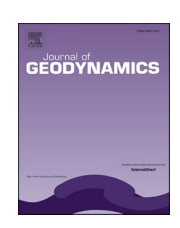
\$ SUPER

Contents lists available at ScienceDirect

Journal of Geodynamics

journal homepage: www.elsevier.com/locate/jog





A simple picture of mantle wedge flow patterns and temperature variation

Ikuko Wada

Department of Earth and Environmental Sciences, University of Minnesota, 116 Church Street SE, Minneapolis, MN, 55455, USA

ARTICLE INFO

Keywords:
Mantle wedge flow pattern
Mantle wedge temperature
Subduction
Arc
Subduction obliquity
Slab geometry
Margin curvature
Numerical subduction models

ABSTRACT

The solid-state mantle flow is an important factor that controls the mass and heat transfer in the solid Earth. This study aims to provide a simple picture of three-dimensional (3-D) mantle flow patterns in the sub-arc region of subduction zones based on the results of 3-D steady-state numerical models with varying subduction parameters. Here, the mantle wedge flow pattern is evaluated based on the azimuthal directions of the mantle inflow from the back-arc and the down-dip outflow. The outflow direction generally parallels the subduction direction, but the inflow direction relative to the outflow direction depends on the local subduction obliquity - the angle between the subduction direction and the strike-normal axis of the subducting slab. A change in the strike of the slab leads to a change in the obliquity and thus the inflow direction. Such change is common along curved margins as the strike of the slab tends to follow that of the margin, or vice versa. Along convex-arc-ward margins, the mantle inflow is deflected towards the region of lowest obliquity but with reduced vigor due to lower dynamic pressure gradients that partly drive the flow, resulting in a cooler mantle wedge. Along concave-arc-ward margins, the mantle inflow is deflected away from the region of lowest obliquity but with increased vigor, resulting in a hotter mantle wedge. These effects increase with decreasing radius of curvature. Along-margin change in the dip of the subducting slab also affects the inflow direction through its impact on the strike of the slab, but its effect is relatively small. We express the azimuthal inner angle between the inflow and outflow directions as a function of obliquity and apply the function to predict sub-arc mantle inflow directions in the circum-Pacific and neighboring regions. Within and among these margins, the inner angle varies over its full range of 0-180°. Most of the margins that are 1000s of kilometers in length are either straight or curved concave-arc-ward with large radii of curvature, for which small or gradual along-margin changes in the mantle inflow direction and the mantle wedge temperature are predicted. A large drop in the mantle wedge temperature by up to a couple of hundred degrees is predicted at short convex-arc-ward segments, such as at the Kuril-Japan and Bonin-Mariana junctions. The fringes of flat slab segments are curved with small radii of curvature, likely resulting in sharp lateral changes in the inflow direction and the mantle wedge temperature.

1. Introduction

The solid-state creeping flow of the mantle is a critical factor in the thermal, chemical, and mechanical evolution of the Earth. Mantle flow patterns at both global and regional scales are complex as they depend on a number of factors, such as driving forces, temperature, density, composition, and rheology, in a non-linear fashion (e.g., Conrad et al., 2007; Alisic et al., 2012; Menant et al., 2016; Schellart, 2017; Stadler et al., 2010). Mantle flow patterns in subduction zones are particularly of significant interest as they affect many important physical processes, including devolatilization of the subducting lithosphere, earthquakes, magma migration and arc volcanism (e.g., Cerpa et al., 2017; Hacker et al., 2003; van Keken et al., 2011; Wilson et al., 2014), but involve added complexity of the subducting lithosphere (e.g., Kneller and van

Keken, 2008; Jadamec and Billen, 2010; Honda et al., 2010; Faccenda and Capitanio, 2012, 2013; Ji and Yoshioka, 2015; Plunder et al., 2018). Against this backdrop, this study aims to provide a simple picture of mantle flow patterns in the sub-arc region of the overriding mantle wedge and their effects on the mantle wedge temperature.

One of the pieces of evidence that the sub-arc mantle participates in the solid-state mantle flow is the occurrence of volcanism, which requires a hot condition for melt generation. However, geophysical observations, such as low surface heat flow in the forearc (e.g., Honda, 1985; Furukawa, 1993; Currie et al., 2004) and low seismic attenuation in the overriding mantle wedge corner (e.g., Stachnik et al., 2004; Rychert et al., 2008; Eberhart-Phillips et al., 2008), indicate that the shallow part of the mantle wedge is cold, which has been largely interpreted to indicate that the mantle is stagnant and decoupled from

E-mail address: iwada@umn.edu.

the subducting slab. The shallow slab-mantle decoupling is generally attributed to the presence of weak hydrous minerals, such as talc, and high pore fluid pressure (e.g., Abers et al., 2006; Hilairet et al., 2007; Hirauchi et al., 2013). Global studies of subduction zone thermal structures indicate that the maximum depth of slab-mantle decoupling (MDD) is 70–80 km for most subduction zones (Wada and Wang, 2009; Syracuse et al., 2010; Abers et al., 2017). Down-dip of the MDD, mechanical coupling between the subducting slab and the overlying mantle largely drives the solid-state flow in the sub-arc region; the mantle immediately above the slab is dragged down-dip, and hot mantle from the back-arc region flows in to replenish the sub-arc region.

Here, we use the mantle wedge inflow and outflow directions to describe the flow pattern. The outflow direction generally parallels the subduction direction regardless of subduction parameters as the outflow is coupled with the subducting slab. As will be shown below, the main factor that determines the inflow direction is the local subduction obliquity, which we define as the angle between the subduction direction and the strike-normal axis of the subducting slab at the MDD (Fig. 1). If the subduction direction parallels the strike-normal axis of the slab, the obliquity is zero (i.e., normal subduction), and the mantle flows in and out parallel to the subduction direction, resulting in a twodimensional flow pattern (Fig. 1a). However, in most subduction systems, the subduction direction is oblique to the strike-normal axis of the slab (e.g., DeMets et al., 2010; Philippon and Corti, 2016), resulting in three-dimensional flow patterns and along-margin mass and heart transfer (e.g., Kneller and van Keken, 2008; Jadamec and Billen, 2010; Bengtson and van Keken, 2012; Ji and Yoshioka, 2015; Wada et al., 2015; Plunder et al., 2018) (Fig. 1b).

We quantify the change in the mantle wedge flow pattern with subduction obliquity, using a series of generic 3-D subduction models, and provide a simple approach to predicting approximate mantle wedge flow patterns where the subduction obliquity is known. We show that along-margin change in the mantle flow pattern occurs where the margin is curved because of the accompanied changes in the strike of the slab and the obliquity. The rate of subduction and the dip angle of the subducting slab are critical parameters that control the kinematics and the vigor of mantle wedge flow and therefore the temperature in the mantle wedge, but their effects on the mantle wedge flow pattern are relatively small.

2. Method

Following Wada et al. (2015), we model steady-state mantle wedge flow in a generic subduction system over a range of subduction obliquity, margin shape, and slab geometry, using the finite-element code PGCtherm3D. All models consist of four components: a subducting slab with kinematically prescribed motion, a non-deforming overriding crust, a non-deforming corner of the overriding mantle wedge, and the rest of the mantle wedge that is viscous (Fig. 2). The transition from a non-deforming wedge corner to viscous mantle is set to occur where the slab surface is at 75-km depth, corresponding to the MDD (Wada and Wang, 2009; Syracuse et al., 2010). Mantle flow velocities in the viscous mantle wedge are computed by solving the equations of conservation of mass and momentum for an incompressible Boussinesq fluid,

$$\nabla \cdot \mathbf{v} = 0 \tag{1}$$

$$\nabla \cdot \mathbf{\sigma}' - \nabla P = 0 \tag{2}$$

where ${\bf v}$ is the flow velocity, ${\bf \sigma}'$ is the deviatoric stress tensor and P is dynamic pressure generated by mantle flow. Temperature within the entire model domain is computed by solving the equation of conservation of energy

$$\nabla \cdot (k\nabla T) - \rho c_p(\mathbf{v} \cdot \nabla T) + Q_H = 0 \tag{3}$$

where k is thermal conductivity, ρ is density, and c_p is specific heat, and Q_H is the volumetric heat production. A uniform thermal conductivity of 3.1 W m $^{-1}$ K $^{-1}$ is used, and the effects of radiogenic heat production and frictional heating are excluded (i.e., $Q_H=0$). The geotherm for the subducting plate at the trench-side vertical is calculated by using the GDH1 plate cooling model (Stein and Stein, 1992) for an intermediate plate age of 30 Myr unless otherwise stated. The geotherm on the back-arc side vertical boundary is calculated based on back-arc surface heat flow of 80 mW m $^{-2}$ (Currie and Hyndman, 2006), mantle potential temperature of 1350°C, and adiabatic temperature gradient of 0.3°C km $^{-1}$, following the approach of Currie et al. (2004).

For the mantle wedge, we apply the dislocation-creep rheology for wet olivine that is reported by Hirth and Kohlstedt (2003), for which the effective viscosity is defined as

$$\eta = \left(AC_{OH}^{r}\right)^{-\frac{1}{n}} \dot{\varepsilon}_{E}^{\left(\frac{1-n}{n}\right)} \exp\left(\frac{E+PV}{nRT}\right) \tag{4}$$

where A and n are constants, $\dot{\varepsilon}$ is the second invariant of strain rate tensor, C_{OH} represents water content, r is water exponent, E is activation energy, V is activation volume, and R is the universal gas constant (8.3145 J mol $^{-1}$ K $^{-1}$). The effect of pressure is small for the sub-arc region and is neglected in this study. We use the following rheological parameter values in all models: $A = 3.0 \times 10^{-20} \, \mathrm{Pa}^{-n} \, \mathrm{s}^{-1}$, n = 3.5, $C_{OH} = 1.0 \, \mathrm{m}^{-1}$

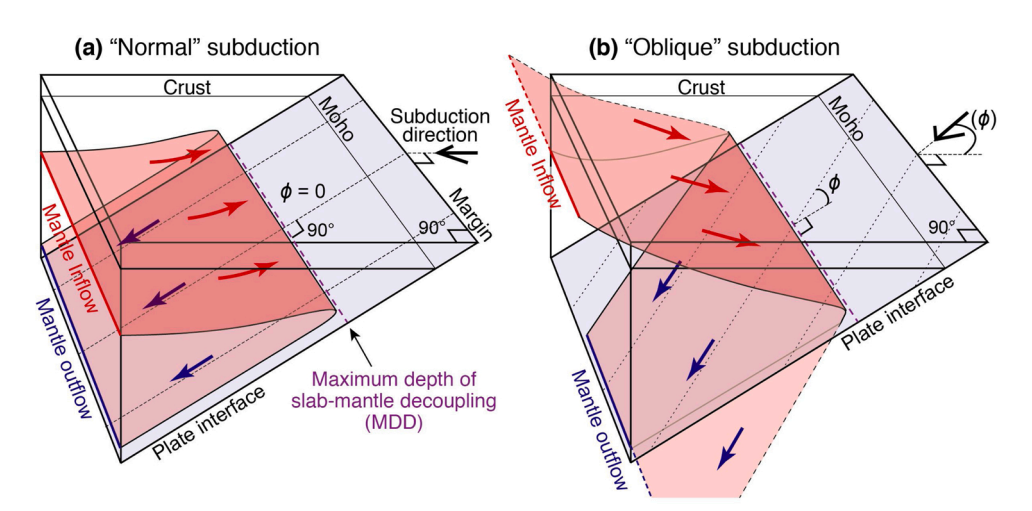


Fig. 1. Schematic diagram illustrating the directions of mantle wedge inflow (red arrows) and outflow (blue arrows) when the subduction direction is (a) normal and (b) oblique to the margin. Red translucent plane represents a surface that is defined by streamlines that pass close to the maximum depth of decoupling (MDD). The local subduction obliquity (ϕ) at the MDD is identical to that at the surface if the strike of the margin is the same as that of the slab at MDD as in the case here.

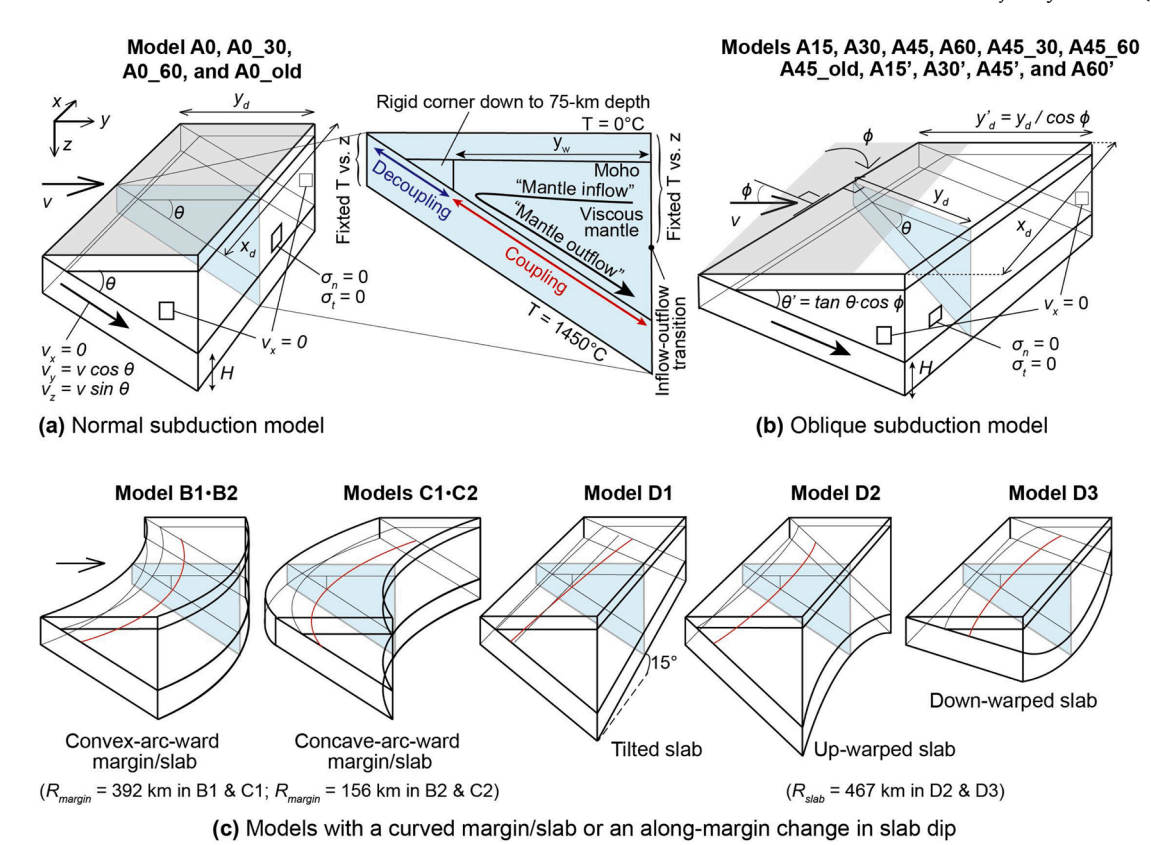


Fig. 2. Model geometry for **(a)** normal subduction, **(b)** oblique subduction, and **(c)** subduction zones with carved margin or along-margin variation in slab dip. Boundary conditions are indicated in **(a)** and **(b)**. All models with 45° slab dip share the same margin-normal vertical cross-sectional geometry at $x = \frac{1}{2}x_d$ (blue shaded area). Oblique subduction models in **(b)** are constructed by rotating the strike of the margin by the specified subduction obliquity (ϕ) and adjusting the model width (y_d) and the apparent slab dip (θ') to achieve the common cross-sectional geometry at the center. Model IDs without the prime symbol (e.g., A15) indicates subduction rate of $v = v_0 = 5$ cm/yr, and those with the prime symbol (e.g., A15') indicate a modified subduction rate of $v = v' = (v_0 / \cos \phi)$ cm/yr. In **(c)**, red line indicates the tip of the flowing part of the mantle wedge that is used to define the local strike of the slab, and R_{margin} and R_{slab} indicate the radius of curvature that is used to define the shapes of the margin and the slab at the back-arc-side boundary, respectively.

1000 H/10⁶Si, and $E = 4.80 \times 10^5 \text{ J mol}^{-1}$.

To quantify the effect of oblique subduction, we use simple models with a straight margin and a straight slab with a uniform dip angle of 45° and vary the obliquity from 0° to 60° at an increment of 15° (Models A0, A15, A30, A45, and A60) (Fig. 2a, b; Table 1). The trench-side vertical boundary is placed where the incoming plate intersects with the overlying plate (i.e., the margin) and is parallel to the x axis for normal subduction models (Fig. 2a). For oblique subduction models, the margin is rotated by the specified subduction obliquity (ϕ) about the z axis (Fig. 2b). The location of the back-arc-side vertical boundary depends on the slab dip and is placed at a 150-km margin-normal horizontal distance (y_w) from the location of the MDD on the slab surface. Zero-shear and zero-normal stress boundary conditions are applied to the back-arcside boundary, and the mantle flows in and out across it. The two sideboundaries are placed parallel to the subduction direction (y axis), and no flow is allowed across these boundaries (i.e., free slip condition). The apparent slab dip (θ ') measured along the side boundaries is \tan^{-1} ($\tan \theta$ $\cos \phi$) where θ is the true dip angle measured normal to the margin. To test the effects of slab dip, we include two pairs of models: one with 30° dip (Models A0_30 and A45_30) and the other with 60° dip (Models A0_60 and A45_60). To test the effects of slab age, we apply a geotherm calculated for a 130 Myr plate age to the trench-side vertical boundary in two additional models (Models A0 old and A45 old).

In one set of models, we apply a subduction velocity (ν) of $\nu_0=5$ cm/yr to the slab. In the case of oblique subduction, the convergence direction should be rotated from the horizon to the down-dip direction about the strike of the slab to obtain the precise subduction direction (Ji and Yoshioka, 2015). However, for easier comparison of the modeling results,

we define the subduction direction to be parallel to the y-axis in all models. With a common subduction rate v_0 , the margin-normal component of the subduction velocity (i.e., $v \cos \phi$) and the sinking rate of the subducting slab (i.e., the vertical component of the subduction velocity; v $\cos \phi \sin \theta$) decrease with subduction obliquity, resulting in a decrease in the down-dip advective heat transfer by the subducting slab. To better understand the effect of subduction velocity, we develop another set of oblique subduction models with a modified subduction rate of $v' = v_0 / \cos v$ ϕ , which allows a common margin-normal component of the subduction velocity of 5 cm/yr regardless of subduction obliquity, resulting in a common sinking rate of the slab for models with the same slab dip. These models are indicated by the prime symbol on the model ID (i.e., A15', A30', A45', and A60'). The common sinking rate minimizes the variation in the down-dip advective heat transport by the subducting slab among the models although it results in an increase in the magnitude of the velocity of the mantle wedge flow with subduction obliquity. The additional velocity magnitude contributes to the along-margin component of mantle wedge flow and thus along-margin transport of heat, which, however, does not impact the mantle wedge temperature as much as the margin-normal component of mantle wedge flow, as shown in Section 3.3.

We develop two models with a convex-arc-ward margin with relatively large and small radii of curvature (Models B1 and B2, respectively; Fig. 2c). Model B1 is constructed such that the margin has a 100° opening over the 600-km model length along the x axis, resulting in a radius of curvature (R_{margin}) of 392 km. The strike of the margin or the subduction obliquity changes from 0° at the center of the model (i.e., x=300 km) to $\pm 50^\circ$ at the side boundaries. In Model B2, the margin curvature has an 80° opening over a 200-km distance between x=200 km

Table 1 Model input parameters (ϕ , v, θ , θ ', and slab age), model-predicted inflow-outflow inner angle (χ), and sub-arc temperature for the normal and oblique subduction models (Model A) and models with a curved margin (Models B and C) or along-margin variation in slab dip (Model D).

Model ID	Obliquity (ϕ , $^{\circ}$)	Subduction rate (ν, cm/yr)	True slab dip $(\theta, ^{\circ})$	Apparent slab dip ⁴ (θ', \circ)	Slab age (Myr)	Inner angle (χ , $^{\circ}$)		Sub-arc temperature (°C) ⁵		
						Stream-line 99	Stream-line 90	80-km depth	90-km depth	100-km depth
A0	0	5	45	45	30	0	0	1307.63	1204.98	812.39
A0_30	0	5	30	30	30	0	0	1333.49	1209.85	835.86
A0_60	0	5	60	60	30	0	0	1279.59	1146.76	797.48
A0_old	0	5	45	45	130	0	0	1308.74	1189.53	723.15
A15	15	5	45	40.89	30	18.48	19.93	1306.78	1202.07	813.22
A30	30	5	45	40.89	30	37.75	41.05	1303.83	1191.93	815.35
A45	45	5	45	35.26	30	57.36	63.03	1296.72	1170.54	820.03
A45_30	45	5	30	22.21	30	55.23	65.63	1314.79	1161.90	844.81
A45_60	45	5	60	50.77	30	52.62	57.81	1272.82	1128.78	803.46
A45_old	45	5	45	35.26	130	54.25	61.69	1298.48	1149.66	725.38
A60	60	5	45	26.57	30	77.83	86.77	1276.79	1126.84	829.02
A15'	15	5.18	45	40.89	30	18.52	19.97	1308.53	1208.04	812.12
A30'	30	5.77	45	40.89	30	38.14	41.42	1311.12	1216.67	810.79
A45'	45	7.07	45	35.26	30	58.81	64.57	1314.97	1230.07	809.06
A60'	60	10	45	26.57	30	82.48	91.80	1318.40	1244.90	807.13
B1	14.79^{1}	5	45 ³	45	30	26.62		1290.62	1190.04	805.91
B2	16 ²	5	45 ³	45	30	39.34		1320.22	1217.59	818.74
C1	14.79 ¹	5	45 ³	45	30	12.10		1235.83	1136.82	780.99
C2	16 ²	5	45 ³	45	30	7.25		1333.47	1230.90	824.34
D1	5.01^3	5	45 ³	32.60-53.68	30	3.19		1308.24	1205.28	813.11
D2	4.55 ¹	5	45 ³	45-56.13	30	2.22		1303.03	1202.41	811.71
D3	5.02^{1}	5	45 ³	27.04–45	30	3.22		1311.84	1210.94	816.43

¹ The obliquity is evaluated at x = 400 km.

and 400 km, with $R_{margin} = 156$ km. For $0 \le x \le 200$ km and 400 km $\le x \le 600$ km, the margin has a uniform strike of 40° and -40° , respectively. In Models C1 and C2, the margins are curved concave-arc-ward and are mirror-images of the margins in Models B1 and B2 about the x-axis, respectively. A constant apparent slab dip of 45° is used in these four models. In another model, a slab is tilted by 15° along the back-arc-side boundary (Model D1). In two models, the slab is either up-warped

(Model D2) or down-warped (Model D3), and the vertical opening angle of the slab at the back-arc-side boundary is 80° in both cases, resulting in $R_{slab}=467$ km. In Models B–D, the back-arc-side vertical boundary is placed parallel to the margin.

All models in this study are 600-km long in the x-direction, and the overriding crust is 35-km thick. The apparent thickness of the slab (H) measured vertically is 95 km for the slab dip of 45° and is adjusted in

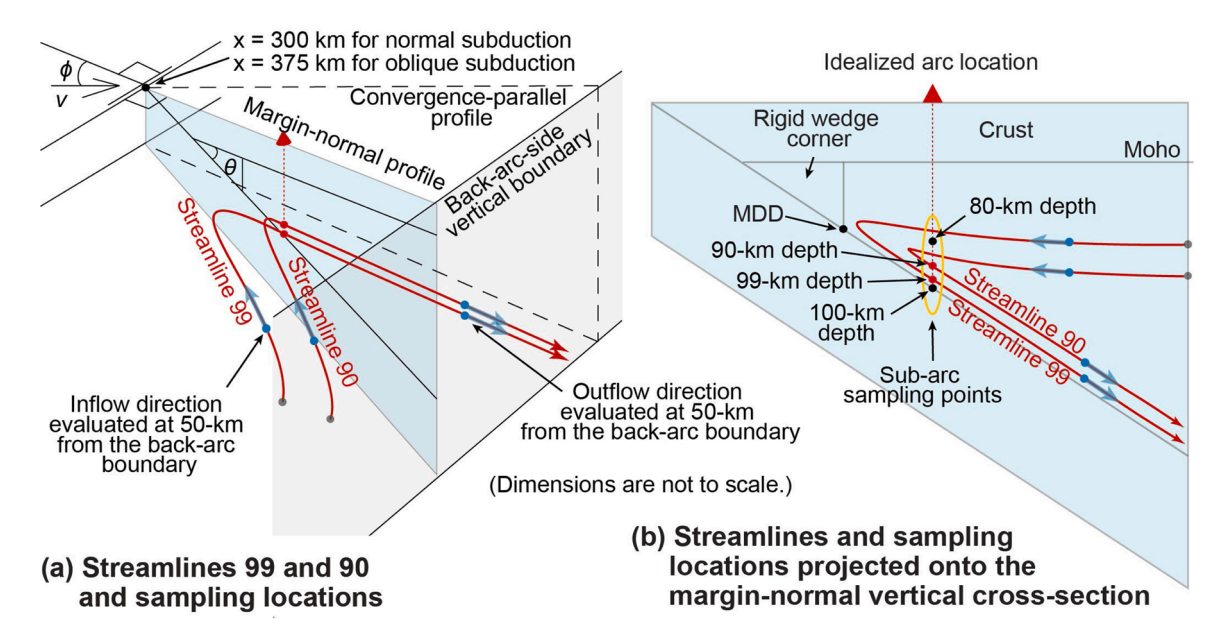


Fig. 3. Schematic diagrams, illustrating the streamlines (red lines) that are used to quantify the azimuthal directions of mantle inflow and outflow and their depths beneath the idealized arc location (blue circles) for oblique subduction models: (a) 3-D view and (b) 2-D projection on the margin-normal vertical cross-section. Translucent blue arrows indicate the inflow and the outflow vectors that are used to represent the inflow and the outflow directions for the streamlines. Sampling points for the sub-arc mantle temperature at the depths of 80, 90, and 100 km are also indicated in (b).

² The obliquity is evaluated at x = 347 km.

³ The obliquity or the slab dip is evaluated at x = 300 km.

⁴ The apparent slab dip is measured parallel to the *y*-axis.

⁵ The sub-arc temperature is measured on a vertical cross-section at x = 375 km for the oblique subduction models and x = 300 km for normal subduction models and models with a curved margin or along-margin variation in slab dip.

models with a slab dip of 30° and 60° (i.e., Models A0_30, A0_60, A45_30, and A45_60) such that it shares the same slab-normal temperature profile with the model with 45° dip. The model parameters are summarized in Table 1.

To quantitatively assess how the inflow and the outflow azimuthal directions vary spatially and with subduction obliquity, we use two streamlines from each model calculation: one is located near the outermost part of the flowing mantle wedge, and the other is located further into the interior of the mantle wedge (Fig. 3a). These streamlines pass through 99-km and 90-km depths, respectively, within a relatively thin outflow region (~85–100 km depths) beneath an idealized arc location in each model and are referred to as Streamlines 99 and 90, respectively. The idealized arc location is defined as the point below which the subducting slab surface lies at 100-km depth, which is approximately the global average location of volcanic arcs (England et al., 2004; Syracuse and Abers, 2006). Along each of these streamlines, we calculate the inflow and outflow azimuthal directions at 50-km away from the back-arc-side vertical boundary to minimize the effect of the boundary condition (Fig. 3). To quantify the effects of subduction

obliquity on mantle wedge temperature, we compare the sub-arc mantle temperature at depths of 80, 90, and 100 km (Fig. 3b).

3. Modeling results

3.1. Subduction obliquity

In the normal subduction model, the mantle flows in and out parallel to the subduction direction, resulting in a two-dimensional flow pattern, for which the inflow and outflow parts of streamlines overlap in a map view (e.g., Model A0; Fig. 4a–c). In the oblique subduction models, the horizontal projections of the inflow and outflow streamlines are not parallel to each other, indicating a three-dimensional flow pattern (e.g., Model A30'; Fig. 4d–f). The inflow direction varies along the margin in the oblique models despite the uniform subduction parameters. This occurs due to the effect of the free slip boundary condition on the side vertical boundaries (i.e., at x=0 and 600 km), which forces the inflow to be parallel to the boundary. This artificial flow along the side boundaries induces dynamic pressure gradients that causes the vigor of

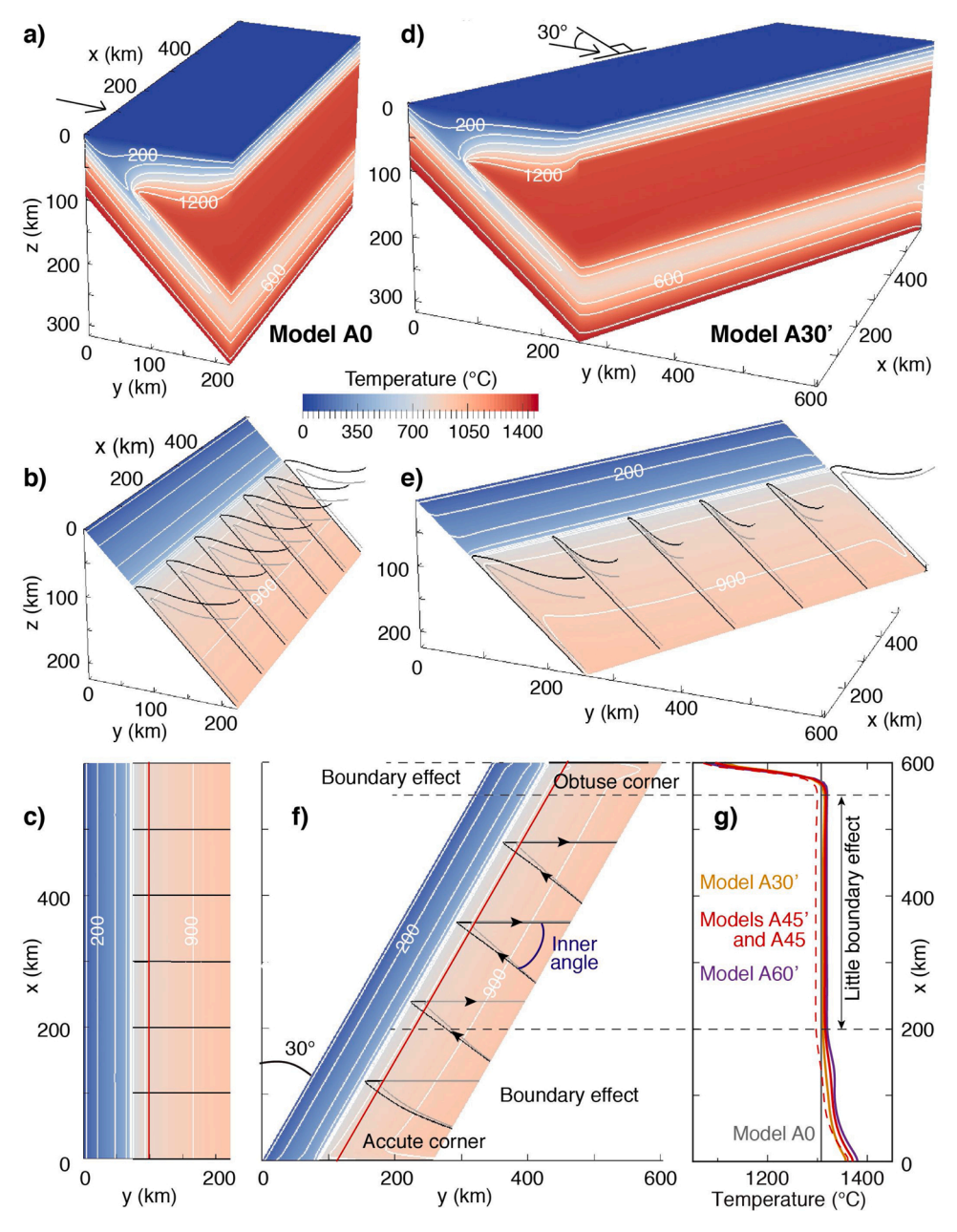


Fig. 4. (a-c) Normal subduction model (ModelA0) and (d-f) oblique subduction model with $\phi = 30^{\circ}$, $\theta = 45^{\circ}$, and the modified subduction rate v' (Model A30'), showing (a, d) the temperature (color) on the outer surfaces of the model, (b, e) the slab surface temperature (color) and Streamlines 99 and 90 (black and grey lines, respectively; Fig. 3), and (c, f) the map view of (b, e), and (g) sub-arc mantle temperature at 80-km depth in Models A0 (solid grey), A30' (solid orange), A45' (solid red), A45' (dashed red), and A60' (solid purple). Red lines in (c, f) indicate the idealized arc location. White lines indicate temperature contours at every 200 °C in (a, b) and every 100 °C in (c-f). Models with v' are used in (g) as they provide a common sinking rate, which minimizes variation in the thermal state of the slab (see Sections 2 and 3.3).

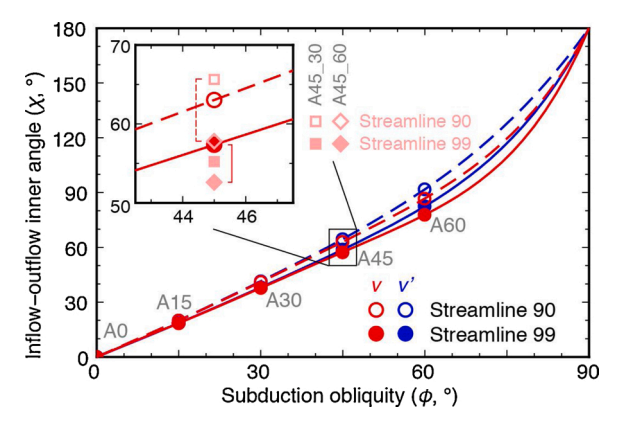


Fig. 5. Change in the inflow-outflow inner angle (χ) with subduction obliquity (ϕ) . Red and blue circles indicate the inner angles that are predicted by Models A0–A60 $(\nu=5\text{ cm/yr})$ and Models A0'–A60' $(\nu'=\nu_0$ / $\cos\phi)$, respectively. Solid and dashed red lines indicate Eqs. 5 and 6, respectively, based on Models A0–A60. Solid and dashed blue lines indicate Eqs. 7 and 8, respectively, based on Models A0'–A60'. In the insert, square and diamond symbols indicate the inner angle predicted by models with $\theta=30^\circ$ and 60° (Models A45_30 and A45_60), respectively. Solid and open symbols are inner angles for Streamlines 99 and 90, respectively. Vertical solid and dashed lines indicate the range of inner angle for $30^\circ \le \theta \le 60^\circ$ for Streamlines 99 and 90, respectively. Models IDs are indicated in grey.

the inflow to increase in the acute wedge corner and decrease in the obtuse wedge corner, leading to a hotter and a cooler condition, respectively (Fig. 4f), as reported by Wada et al. (2015). This boundary effect, however, diminishes within a 200-km distance from the acute corner and a 50-km distance from the obtuse corner for a range of subduction obliquity as indicated by a relatively uniform mantle wedge temperature for 200 km < x < 550 km in Fig. 4g. For the following, we report the results from the central part of the model domain where the effect of boundary effect is negligible.

In contrast to the inflow direction, the outflow direction does not vary significantly with the choice of the streamline or the sampling location along the streamline, and it is nearly identical to the subduction direction with a difference that is generally much smaller than a fraction of a de-

gree. Below, we use the azimuthal inner angle (γ) between the inflow direction and the subduction direction (i.e., parallel to the y-axis) as the inflow-outflow inner angle and quantify its variation with subduction obliquity and other factors, such as the choice of streamlines and slab dip (Fig. 5; Table 1). For a given streamline and subduction rate, the increase in the inner angle with subduction obliquity appears roughly linear for ϕ $< 60^{\circ}$, but there is a small uptick in the slope with subduction obliquity, indicating slight nonlinearity. Here, we include a theoretical inner angle of 180° for 90° obliquity, where the subducted part of the plate no longer sinks but moves laterally with respect to the overriding plate. Such scenario is likely applicable near the western end of the Aleutians and the northern end of Sumatra. This theoretically expected inner angle indicates that the increase in the inner angle is strongly nonlinearly at high subduction obliquities although the details of the nonlinearity is difficult to verify due to the extremely high resolution that is required to overcome numerical instabilities that are associated with high subduction obliquity. Polynomials of degree 5 are fitted to the five model-predicted inner angles for Streamlines 99 and 90 and the additional theoretical inner angle of 180° at 90° obliquity, exactly satisfying all inner angles. The relations for Streamlines 99 and 90 for the models with the common subduction rate (v $= v_0 = 5$ cm/yr) (red solid and dashed lines in Fig. 5) are

$$\chi(\phi) = 9.46722 \times 10^{-8} \phi^5 - 1.34065 \times 10^{-5} \phi^4 +6.52016 \times 10^{-4} \phi^3 - 1.12708 \times 10^{-2} \phi^2 + 1.29495 \phi$$
(5)

and

$$\chi(\phi) = 5.60525 \times 10^{-8} \phi^5 - 7.39103 \times 10^{-6} \phi^4 +3.33759 \times 10^{-4} \phi^3 - 3.58643 \times 10^{-3} \phi^2 + 1.32979 \phi$$
(6)

respectively. The relations for Streamlines 99 and 90 for the models with the common sinking rate (i.e., subduction rate of $\nu' = \nu_0 / \cos \phi$) (blue solid and dashed lines in Fig. 5) are

$$\chi(\phi) = 4.30633 \times 10^{-8} \phi^5 - 4.82986 \times 10^{-6} \phi^4 + 1.90349 \times 10^{-4} \phi^3 - 6.95597 \times 10^{-4} \phi^2 + 1.21637 \phi$$
(7)

and

$$\chi(\phi) = 2.87201 \times 10^{-9} \phi^5 + 1.31071 \times 10^{-6} \phi^4 - 1.22396 \times 10^{-4} \phi^3 + 6.57411 \times 10^{-3} \phi^2 + 1.25580 \phi$$
(8)

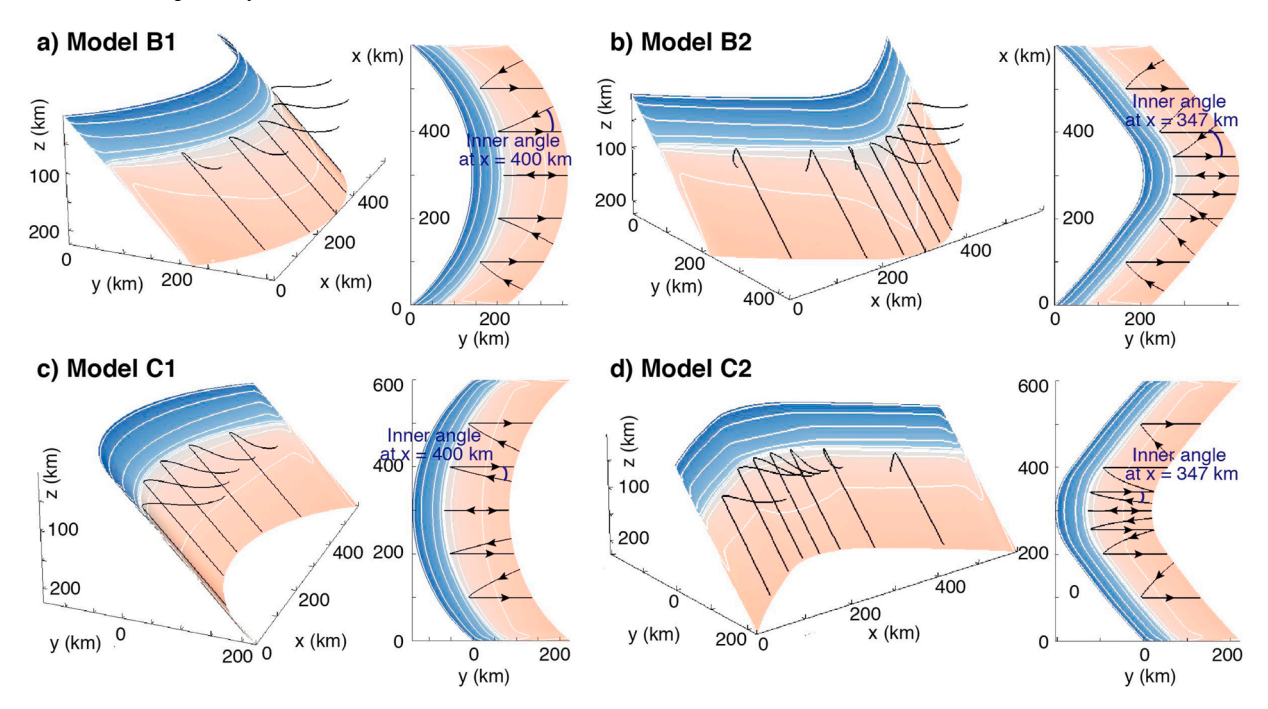


Fig. 6. (a-d) 3-D view (on the left column) and the map view (on the right column) of the slab surface temperature (color) and Streamlines 99 (black lines) in models with a curved margin (Models B-C).

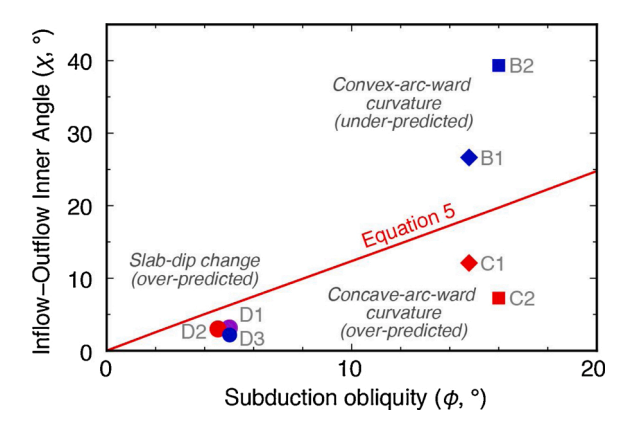


Fig. 7. Inflow-outflow inner angle (χ) plotted against local subduction obliquity (ϕ) in models with a convex-arc-ward margin (Model B; blue diamond and square), a concave-arc-ward margin (Model C; red diamond and square), a tilted slab (Model D1; purple circle), an up-warped slab (Model D2; red circle), and a down-warped slab (Model D3; blue circle). The red line represents Eq. 5, indicating the effect of obliquity without along-margin variation in subduction geometry.

respectively. Given that the inflow direction is spatially variable even along a given streamline and that the above relations are specific to the prescribed subduction geometry, kinematic forcing, and thermal parameters, these relations are not intended to provide precise mantle flow directions but to help understand the general pattern of the inflow direction relative to the outflow direction.

In the case of uniform subduction obliquity, the inner angle is always greater than the obliquity but no greater than twice the obliquity. For a given model, the inner angle is larger by several degrees along the streamline that is further into the interior of the mantle wedge, peaking at $70-75^{\circ}$ obliquity (e.g., peak difference of 10.49° between red solid and dashed lines at 71.6° obliquity in Fig. 5). The effect of slab dip is relatively small; the inner angle increases by a few degrees for Streamline 99 and several degrees for Streamline 90 as slab dip increases from 30° to 60° for models with 45° obliquity (insert in Fig. 5). The inner angle also increases with subduction rate, but the difference of $\sim 5^{\circ}$ between Models A60 and A60' for both streamlines, despite the difference in the subduction rate by a factor of 2, indicates that the impact of subduction rate is also relatively small. The modeling results indicate that the effect of the slab age is also small; the difference in the inner angle between Models A45 and A45 old is only a few degrees for both streamlines (Table 1).

3.2. Margin curvature and slab geometry

The subduction obliquity that affects the mantle wedge flow pattern is measured relative to the strike-normal axis of the subducting slab and not to the strike-normal axis of the margin. However, because the strike of the margin often, although not always, follows the strike of the slab, or vice versa, the shape of the margin relates to the mantle wedge flow pattern indirectly through its relation to the geometry of the slab. Models B-C mimic this situation; the margin is curved either convex arcward or concave arc-ward, and the strike of the slab follows that of the margin at all depths (Fig. 6). In Models B1 and B2 with a convex-arcward margin, the mantle inflow from the side flanks of the slab is deflected towards the center of the model (i.e., x = 300 km) where the obliquity is lowest (Fig. 6a,b). In Models C1 and C2 with a concave-arcward margin, the inflow is deflected away from the center of the model (Fig. 6c,d). Due to the deflection of the mantle inflow, the inflowoutflow inner angle for a given local obliquity is greater at convex margins and smaller at concave margins, compared to the straight margin with a constant obliquity (Fig. 7). For example, at x = 400 km where the obliquity is 14.79° in Models B1 and C1, the inner angle is 26.62° and 12.10°, respectively, for Streamline 99. These values are

under- and over-predicted by Eq. 5, respectively. The deviation of the inner angle from Eq. 5 increases with decreasing radius of curvature.

In Models D1–D3, the along-margin change in the slab geometry is represented by a change in the slab dip without a change in the margin strike (Fig. 8). However, such geometry results in variations in the strike of the slab and subduction obliquity at depth (Figs. 2c and 7). In Model D1, the down-dip end of the slab is tilted by 15°, which results in \sim 5° obliquity and an inflow-outflow inner angle of \sim 3° along the midsection of the model (i.e., x=300 km). In Models D2 and D3, the upwarped and down-warped slab geometries result in convex-arc-ward and concave-arc-ward shapes of the slab, respectively. The resulting mantle flow patterns are similar to models with margin curvature, but the inner angles are smaller than the straight margin with a constant obliquity (Fig. 7), indicating that the lateral variation in the slab dip reduces the impact of subduction obliquity on the inner angle and that the effect of along-margin variation in the slab dip on the mantle wedge flow pattern is small (Table 1).

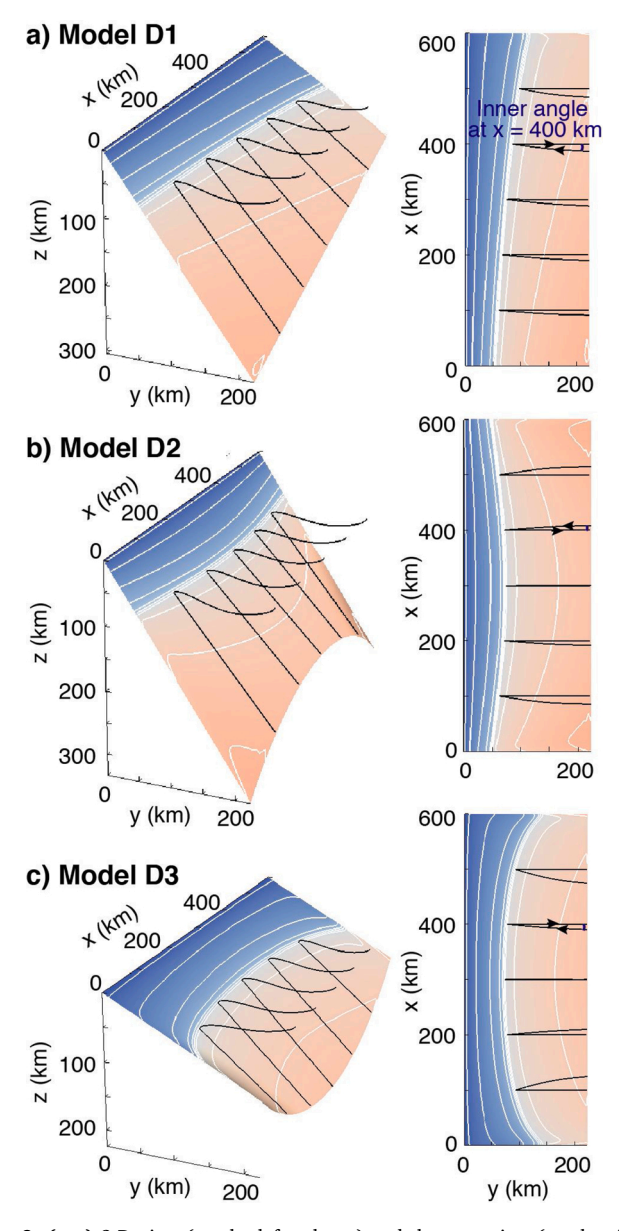


Fig. 8. (a–c) 3-D view (on the left column) and the map view (on the right column) of the slab surface temperature (color) and Streamlines 99 (black lines) in models with along-margin variation in slab dip (Models D1–D3, respectively).

Eqs. 5–8 are meant to provide a first-order approximation to the mantle inflow direction. The approximation degrades with increasing curvature of the margin or the slab, but the comparison of the equations with the results for curved margins and slabs provides the sense of the impact of margin/slab curvature on the inner angle. A parametrization for the inner angle as a function of the curvature would be useful, but the inflow direction at a curved margin depends not only on the curvature but also subduction obliquity, which varies along the margin. Parameterizing the inner angle as a function of margin curvature, subduction obliquity, and distance along the margin, would require substantially greater effort. Thus, when one is required to predict the mantle wedge flow pattern along a curved margin with higher accuracy, it is more practical to simply develop a 3-D model for the margin.

3.3. Mantle temperature

Subduction velocity is a critical parameter that controls the mantle wedge temperature as it controls the rate of advective heat transfer. For a given subduction rate and slab dip, a higher subduction obliquity results in a smaller margin-normal component and a larger marginparallel component of the slab motion. The margin-normal component of the velocity brings in hot mantle from the back-arc region, which largely accounts for the advective heat transfer into the sub-arc region, whereas the margin-parallel component is less efficient in bringing in heat. Thus, a higher subduction obliquity results in a cooler mantle wedge for a given subduction rate (i.e., models with $v = v_0$; thin red line in Fig. 9a,b). An increase in obliquity from 0 to 60° results in a decrease in the sub-arc mantle temperature by 30.84 °C at 80-km depth and 78.14 °C at 90-km depth. At the surface of the subducting slab, however, temperature increases with subduction obliquity despite the cooler overriding mantle wedge (Fig. 9c). This occurs because the smaller margin-normal component of the slab motion results in slower sinking of the slab, allowing more diffusive heat transfer from the surrounding hot mantle to the slab, as reported also by Ji and Yoshioka (2015) and Plunder et al. (2018).

The magnitude of the impact of subduction obliquity on mantle wedge temperature is comparable to the effects of slab dip and subduction velocity. For a constant subduction rate, an increase in slab dip tends to decrease the mantle wedge temperature; for example, an increase from 30° to 60° dip causes a decrease in the mantle wedge temperature by a few to several tens of degrees (vertical red dashed lines in Fig. 9a, b). A higher slab dip also causes faster downward advective heat transfer by the slab, resulting in lower slab surface temperature at a given depth (Fig. 9c).

The use of a common sinking rate of the slab (i.e., using the modified subduction velocity of $v=v'=v_0$ /cos ϕ) reduces the variation in the thermal state of the slab with subduction obliquity and thus its impact on the mantle wedge temperature (thin blue line in Fig. 9c). For a constant sinking rate, the temperature in the mantle wedge increases with subduction obliquity. The temperature increase is attributed to the increased margin-parallel component of the advective heat transport within the mantle wedge (red circles in Fig. 9a,b). For a given obliquity, an increase in subduction rate results in a hotter mantle wedge and a cooler slab surface. For example, the sub-arc mantle temperature in Model A60' is higher by 41.61° at 80-km depth and 118.06° at 90-km depth than that in Model A60 (Fig. 9c). Therefore, the subduction rate has a relatively large impact on the mantle wedge temperature unlike its small effect on the inflow-outflow inner angle.

The mantle flow patterns at convex- and concave-arc-ward margins result in a cooler and a warmer mantle wedge, respectively (Figs. 9 and 10). Along convex margins (Models B1 and B2), the deflection of inflow towards the region of lowest obliquity elevates the dynamic pressure, reducing the pressure gradients that partly drive the flow. This results in slower mantle inflow at the center and a cooler condition in the mantle wedge and along the slab surface, as reported by Wada et al. (2015). The deflection of inflow away from the region of lowest obliquity along

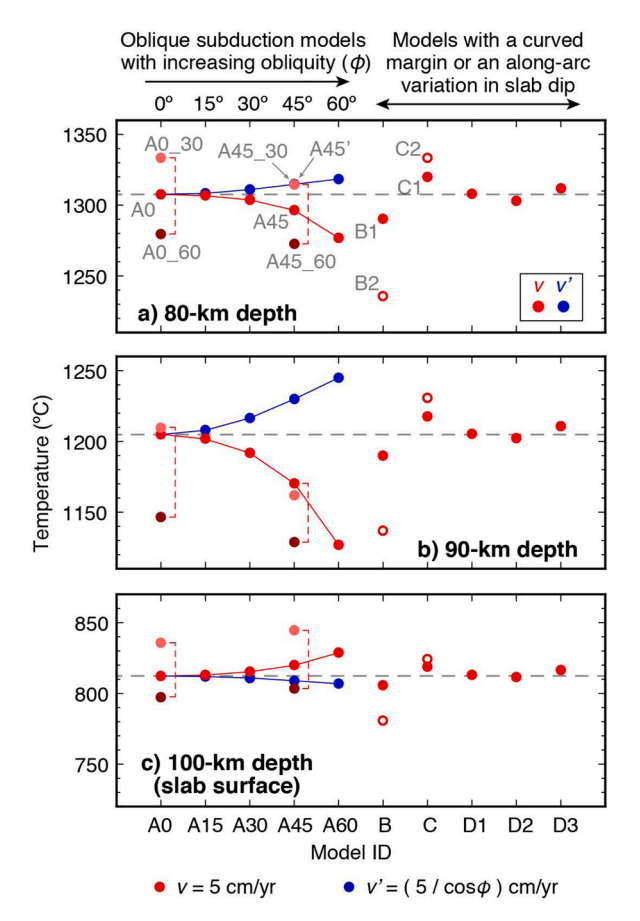


Fig. 9. Sub-arc temperature (red solid and open circles) at the depths of **(a)** 80 km, **(b)** 90 km, and **(c)** 100 km (slab surface) at x=300 km (along the midsection) in the oblique models with obliquity (ϕ) of 0°, 15°, 30°, 45°, and 60° (Models A0–A60, respectively) and models with a curved margin or along-margin variation in slab dip (Models B–D). Blue solid circles indicate sub-arc temperature in the oblique models with a uniform sinking rate (i.e., with a modified subduction rate ν '). Light and dark red circles indicate sub-arc temperature in models with slab dip (θ) of 30° and 60°, respectively (Models A0_30, A0_60, A45_30, and A45_60). Vertical dashed line indicates the temperature variation due to slab dip. Grey numerals indicate model IDs. Grey dashed line indicates the sub-arc mantle temperature at the respective depth in the normal model with θ of 45° (Model A0). The vertical axis in each panel spans 150 °C.

concave margins lowers the dynamic pressure, increasing pressure gradients and the vigor of the mantle inflow. This results in a hotter condition in the mantle wedge and along the slab surface. At both convex and concave margins, their effects are greater for a smaller radius of curvature. In contrast to the effects of margin and slab curvature, along-margin variation in the slab dip alone has a small effect on the mantle wedge temperature (Fig. 9).

4. Global distribution of inflow directions

With the relations between subduction obliquity and the inflowoutflow inner angle in Eqs. 5–8 and the knowledge of how the inflow direction varies along curved margins (Figs. 5 and 7), one can predict the approximate mantle inflow direction and along-margin variation in mantle wedge temperature where the obliquity is known (Fig. 11). We calculate subduction obliquity at selected points that are approximately 500-km distance apart along the circum-Pacific margin, the Ryukyu-Manila-Philippine margin, the Sunda-Java margin, and the Lesser Antilles margins, based on the local subduction direction and strike of the subducting slab at 80-km depth. The subduction directions are based on the relative plate motion model MORVEL (DeMets et al., 2010), and

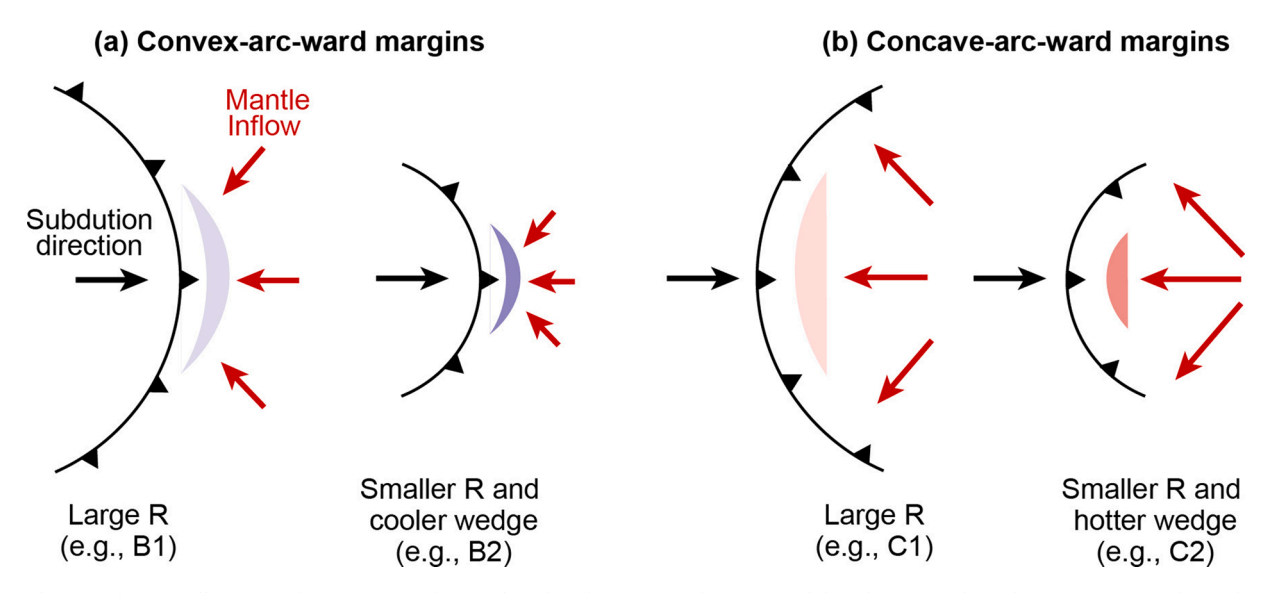


Fig. 10. Schematic diagram, illustrating the variation in the mantle inflow directions (red arrows) and the relative mantle wedge temperature (color of the crescent region) with the curvature of (a) convex-arc-ward and (b) concave-arc-ward margins. Darker blue and red of the crescent region indicate colder and hotter conditions, respectively, in the mantle wedge relative to the mantle wedge with uniform subduction obliquity; the shape does not represent the actual shape of the region with temperature anomalies. The relative vigor of the inflow is indicated by the lengths of the red arrows; the variation in their lengths among different margin shapes is exaggerated.

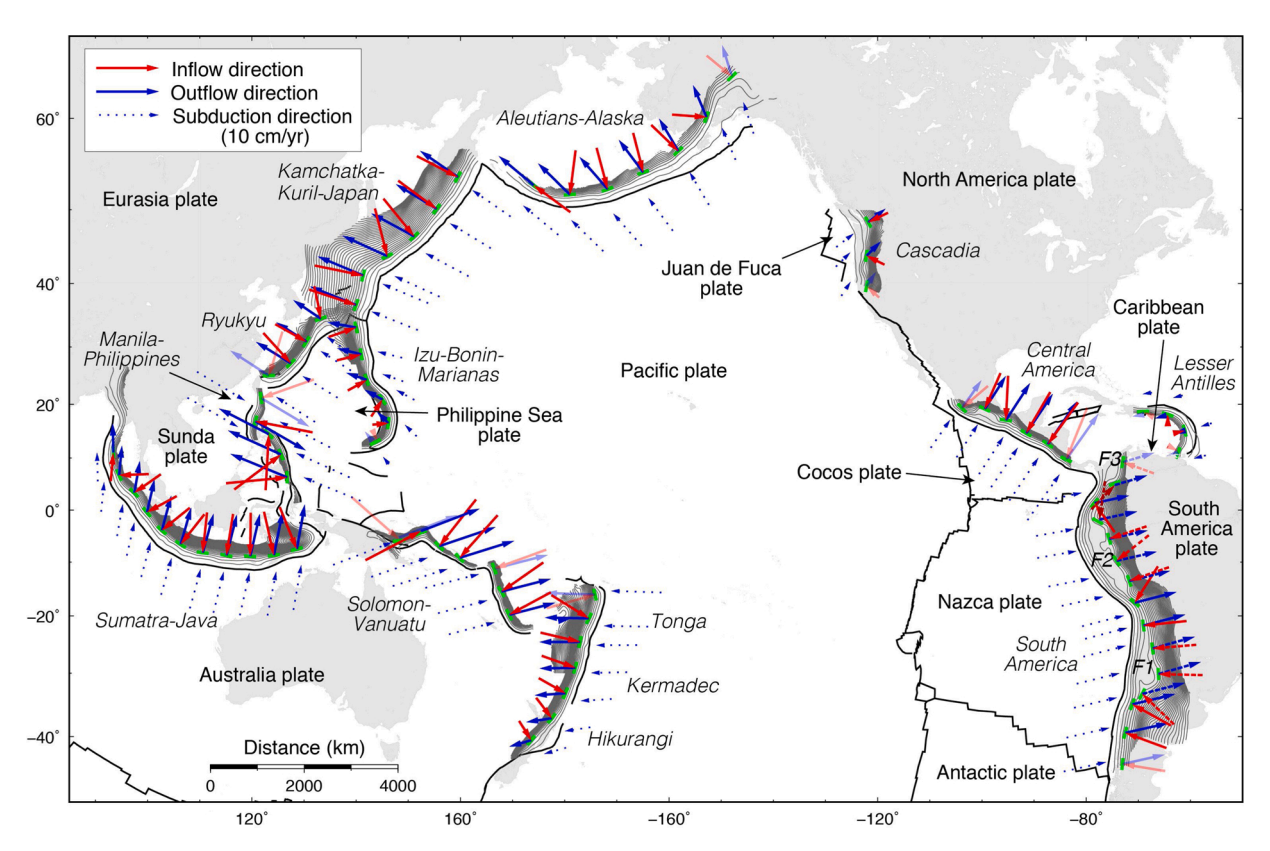


Fig. 11. Sub-arc mantle inflow directions (solid red arrows) in the sub-arc region based on Eq. 5. The obliquity is calculated based on the convergence velocity relative to the overriding plate (dotted thin blue arrows) from MORVEL (DeMets et al., 2010) and the local strike of the subducting slab (thick green line) at 80-km depth from Slab2.0 (thin grey contours) (Hayes et al., 2018). The inflow direction around the Pampean, Peruvian, and Bucaramanga flat-slab segments (F1–F3, respectively; Ramos and Folguera, 2009) are evaluated at 120-km depth (thick dashed red arrows); dark red arrows are used for the inflow directions that are overlapping between the Peruvian and Bucaramnga segments. The convergence direction is used to indicate the approximate mantle outflow direction (thick solid and dashed blue arrows). The magnitudes of the inflow and outflow velocities cannot be determined and are approximated by that of the convergence velocity. The mantle flow pattern around slab edges likely differ significantly from the prediction, and the inflow and outflow directions within a ~200-km distance from a slab edge are indicated by translucent red and blue arrows for reference only (see text for discussion).

the local strike of the slab is based on the slab geometry model Slab2.0 (Hayes et al., 2018). The inflow directions along these margins are calculated by using the local subduction obliquity and Eq. 5, which is for Streamline 99 in models with a subduction rate of 5 cm/yr ($v = v_0$) and a dip angle of 45°. Here, we use Eq. 5 with a constant subduction rate rather than Eq. 7 with a constant sinking rate to illustrate the variation in the mantle flow directions along individual margin segments, within which the subduction rate often does not vary significantly. Deviations of the actual subduction rate and dip angle from the values that are assumed result in uncertainties of up to several degrees in the inflow direction; a faster subduction results in a slightly larger inner angle, and a deeper dip results in a slightly smaller inner angle (Fig. 5). A greater uncertainty in the predicted inflow direction is expected near the edges of the subducting slabs where analog models (e.g., Funiciello et al., 2006; Strak and Schellart, 2014) and numerical models (e.g., Jadamec and Billen, 2010, 2012; Stegman et al., 2010; Király et al., 2017) both predict toroidal flow around the edges, such as beneath Alaska and at the northern end of the Kamchatka margin. The models of Jadamec and Billen (2010) and Faccenda and Capitanio (2012, 2013) that simulate toroidal mantle flow around a slab edge, for example, indicate that the effect of toroidal flow is dominant only within ~100-200 km from the slab edge. In Fig. 11, we indicate the inflow and outflow directions that are within 200 km of a slab edge, using translucent red and light blue arrows, respectively, for future comparison with model predictions that incorporate the effect of a slab edge.

Most of the subduction margins whose lengths are on the order of 1000s of kilometers are either relatively straight (Chile, central America, Kuril, Izu-Bonin, and Tonga-Kermadec margins) or curved concave-arcward with large radii of curvature (Columbia-Ecuador-Peru, Aleutian, Marianas, Ryukyu, Vanuatu and Sumatra-Java margins). Along the straight margins, uncertainties in the predicted inflow direction are attributed largely to deviations of the assumed subduction rate and slab dip from the actual but are expected to be relatively small (up to several degrees) based on the small variation in the inner angle with subduction rate and slab dip (Figs. 5). The inner angles at the large-scale concavearc-ward margins in Fig. 11 are likely over-predicted by Eq. 5 (Fig. 7), but the overprediction is expected to be very minor, by a few degrees, given the large radii. The diverging mantle inflow directions results in very slightly higher mantle wedge temperature (Figs. 9 and 10) compared to neighboring straight segments if present. Within the margin, the warmest region is where the obliquity is at the lowest. However, along-margin changes in the mantle inflow direction and mantle wedge temperature should be small and gradual, given the large radii of curvature.

Between the straight and gently curved long margins, there is often a short segment that is curved convex-arc-ward with small radii of curvature (e.g., between Kuril and Japan in NE Japan, between Marianas and Bonin islands, between Solomon and Vanuatu; those with discontinuous slabs, such as at the Kamchatka-Aleutian junction, should be excluded). At these short convex-arc-ward margin segments, the inflow-outflow inner angles are likely significantly under-predicted given the small radii of curvature, and the rapid along-margin change in the inflow direction, greater than depicted in Fig. 11, is expected. A numerical model for the Kuril-Japan trench junction with a sharp convex arc-ward curvature predicts a converging pattern of the inflow direction and mantle wedge temperatures that are lower by as much as ~200°C than the surrounding gently curved segments (Wada et al., 2015).

Along some margins, the strike of the slab does not follow that of the margin. Among those, sharp curvatures in the slab, both convex and concave, are observed at the fringes of flat-slab segments, such as in Mexico and Pampean, Peruvian, and Bucaramanga segments in South America (e.g., Manea et al., 2017; Ramos and Folguera, 2009) (Fig. 11). The results of this study indicate that the sharp changes in subduction obliquity around the fringes of flat segments result in relatively large along-margin changes in the inflow direction and thus the mantle wedge temperature.

The predicted inflow patterns are generally consistent with those predicted by available 3-D numerical models that are specifically constructed for some parts of subduction zones, including Marianas (Bengtson and van Keken, 2012), NE Japan (Wada et al., 2015; Morishige and van Keken, 2014), Costa Rica and Nicaragua (Rosas et al., 2016), and Nankai (Ji and Yoshioka, 2015). The consistency indicates that along-margin changes in the mantle inflow direction can largely be explained by changes in the subduction obliquity without taking other factors, such as subduction rate and slab dip, into consideration.

Predicting detailed mantle wedge flow patterns, particularly their variations at smaller scale than discussed above, and quantifying their effects on the thermal structures of subduction zones require 3-D numerical models with subduction parameters that are specific to the region of interest. Further, although the assumption of a common MDD seems reasonable at large scale for most subduction zones, some variation in the MDD at local to regional scales may exist, affecting the mantle wedge flow pattern. Similarly, the thermal structure of the back-arc likely varies within and among subduction systems, affecting the temperature and the rheology of the mantle that flows into the sub-arc region, but it is assumed to be uniform in this study. Small-scale convection in the back-arc, for example, result in a laterally heterogeneous thermal structure (Honda and Yoshida, 2005; Honda et al., 2010), which can cause a complex mantle flow patterns that are characterized by alternating vigorous inflow of hot mantle and subdued inflow of cold mantle (Lee and Wada, 2017, 2021). The large-scale concave-arc-ward margin shape has been linked to the lateral variation in the rates of back-arc spreading and slab rollback and also to the interaction of the slab edges with the upward component of the toroidal mantle flow around the slab edges that causes the edges to curl up and the margin edges to move inward (e.g., Morra et al., 2006; Stegman et al., 2010; Schellart, 2017). The effects of these processes on the sub-arc mantle wedge flow pattern at regional scale further add uncertainties to the inflow direction. Hydration and partial melting in the mantle wedge reduce the viscosity of the mantle, also affecting the flow pattern (e.g., Gerya and Yuen, 2003; Arcay et al., 2005; Hebert et al., 2009; Gerya and Meilick, 2011). In particular, higher mantle wedge temperatures at concave-arc-ward margins can lead to a higher degree of melting and lower mantle viscosity, which further focuses the mantle flow and causes even higher temperature than predicted in this study. The effect works in the opposite direction at convex-arc-ward margins, increasing the temperature contrast between concave-arc-ward and convex-arc-ward margins. With a number of factors at play and a lack of direct constraints, predicting detailed mantle wedge flow patterns continues to be a challenge. The result presented here is a simplified view of the mantle wedge flow pattern and temperature variation based on the premise that the slab-mantle coupling is the primary driving mechanism of the mantle wedge flow.

Surface heat flow generally decreases from the trench towards the arc due to the cooling effect of the subducting plate, but it starts to increase near the arc, indicating the presence of the hot asthenospheric mantle that is brought in by the mantle wedge flow (e.g., Furukawa, 1993; Currie et al., 2004; Wada and Wang, 2009). The location of the arc-ward increase in the surface heat flow is strongly dependent on the trench-ward extent of the mantle wedge flow whereas the arc-ward gradient of the increasing surface heat flow depends on the thermal contrast between the cold, stagnant mantle wedge corner and the hot, flowing mantle. Thus, along-margin variation in the mantle wedge temperature due to curvature of the margin or the slab can manifest in the arc-ward gradient in surface heat flow (e.g., Wada et al., 2015). However, in many subduction zones, surface heat flow data are scarce, and even in those with sufficient heat flow data, they are generally highly scattered in the arc region due to hydrothermal activities and magmatic processes, making it difficult to relate the lateral gradient in surface heat flow to relatively small changes in the mantle wedge temperature at present.

The distribution of arc volcanism depends on the production of melts

at depths, which in turn depends on the temperature condition and the availability of aqueous fluids. For a given supply of slab-derived fluids, variation in the mantle wedge temperature can affect the degree of melting (e.g., Gaetani and Grove, 1998; Grove et al., 2006; Till et al., 2012). However, if there are sufficient slab-derived fluids, a reduction in the mantle wedge temperature by $\sim\!200~^\circ\text{C}$ due to margin or slab curvature is unlikely to prevent partial melting completely (e.g., Grove et al., 2006). In fact, over the short convex-arc-ward segment in NE Japan, for which $\sim\!200~^\circ\text{C}$ drop in the mantle wedge temperature is predicted, arc volcanism is active (Wada et al., 2015). As discussed above, other factors, such as along-margin variation in MDD and the dynamics and the thermal structure of the back-arc, impact mantle wedge flow patterns, affecting the distribution of arc volcanoes as well as surface heat flow.

The fringes of flat-slab segments are commonly associated with sharp changes in surface heat flow and spatial gaps or lack of arc volcanoes, all of which are attributed largely to the presence of shallow flat slabs (Manea et al., 2017), and the impact of subduction obliquity at the fringes on lateral changes in heat flow and arc volcanism is yet to be investigated. The quantifying the mantle wedge flow pattern and temperature distribution at the fringes of flat-slab segments, however, can be further complicated by the presence of a tear in the slab, as proposed for the southern end of the Peruvian segment based on seismological observations (e.g., Antonijevic et al., 2016; Wagner et al., 2017). The pressure gradient across a tear is likely to strongly impact the mantle inflow direction.

Model predictions of mantle flow patterns in the upper mantle are often used to explain the fast polarization directions of shear waves by assuming that the mantle flow results in the development of crystal preferred orientation (CPO) of the elastically anisotropic mineral olivine (e.g., Jung and Karato, 2001; Katayama and Karato, 2006; Skemer and Hansen, 2016). With the conventional interpretation of splitting observations that invokes A-type (or D or E-type) olivine CPO, whose fast axis tend to align with the mantle flow direction, model-predicted mantle flow directions are generally consistent with the splitting observations over the ocean basins (e.g., Conrad et al., 2007; Karato et al., 2008; Long and Becker, 2010). However, the fast directions in subduction zones are spatially variable; in many subduction zones, they are margin-parallel in the forearc and arc regions and margin-normal in the back-arc (e.g., Nakajima et al., 2006; Long and Silver, 2008; Long and Wirth, 2013). The model-predicted mantle wedge inflow direction (Fig. 11; Kneller and van Keken, 2008) is generally consistent with the margin-normal fast direction in the back-arc when the conventional interpretation is used. However, the margin-parallel fast direction in the forearc and arc regions is difficult to be explained by the same conventional interpretation. As a consequence, a range of mechanisms have been invoked to explain the fast directions in the forearc and arc regions of subduction zones, including B-type olivine CPO (e.g., Kneller et al., 2005,2008; Katayama and Karato, 2006), CPOs of other upper mantle minerals, such as antigorite (e.g., Katayama et al., 2009), trench-parallel flow associated with a slab edge, a slab tear, and trench motion (e.g., Long and Silver, 2008; Hoernle et al., 2008), the shape preferred orientation of melt lenses (e.g., Holtzman et al., 2003), small-scale convection (e.g., Ishise et al., 2018), and anisotropy in the overriding crust (e.g., Uchida et al., 2020). Even for oblique subduction zones, the model-predicted mantle inflow directions are closer to margin-normal than margin-parallel (Fig. 11), and the margin-parallel fast direction cannot be explained using the conventional interpretation, requiring further investigation on the source of seismic anisotropy in the forearc and arc regions through coordinated efforts on seismic experiments and numerical simulations.

5. Conclusions

In this study, the mantle wedge flow pattern is characterized by an increase in the inflow-outflow inner angle with subduction obliquity

based on the results of 3-D numerical models. For a given obliquity, the inner angle tends to be slightly larger for steeply dipping slab, faster subduction rate, and streamlines that are further into the interior of the mantle wedge. Along-margin change in the inner angle occurs along curved margins, and the mantle inflow tends to converge towards or diverge away from the region with lowest obliquity at convex- and concave-arc-ward margins, respectively. This effect increases with decreasing radius of curvature. Along-margin change in slab dip also affects the inner angle, but its effect is relatively small.

The relations between the inner angle and obliquity are expressed quantitatively, allowing the prediction of the mantle inflow direction for a given subduction obliquity. The relations, however, under-predict the inner angle at convex-arc-ward margins and over-predict the angle at concave-arc-ward margins, and the deviation of the inner angle from the predicted increases with decreasing radius of curvature. Further, subduction obliquity due solely to along-margin change in slab dip results in inner angles that are smaller than the predicted.

Most of the subduction margins that are 1000s of kilometers in length are either relatively straight or gently curved concave-arc-ward. Along such margins, the lateral variations in the mantle flow pattern and the mantle wedge temperature are expected to be small. These long margins are often bounded by short margin segments that are curved convex arc-ward with small radii of curvature, where the inflow direction and the mantle wedge temperature likely change significantly. Further, sharp changes in the strike of the slab at the local scale, such as at the fringes of flat slab segments, can result in rapid along-margin changes in the inflow direction and mantle wedge temperature. Large uncertainties remain in the mantle wedge flow patterns as they are influenced by a number of factors, such as the effects of slab edges, slab rollback, and the dynamics and the thermal structure of the back-arc mantle. However, quantifying the variation in the inflow direction with subduction obliquity helps to provide a better understanding of mantle wedge flow patterns.

Author statement

Ikuko Wada: Development of the rationale and design of the study, simulations and analyses of numerical models, visualization, writing, reviewing, and editing.

Declaration of Competing Interest

The authors declare that they have no known competing financial interests or personal relationships that could have appeared to influence the work reported in this paper.

Acknowledgements

I thank J. He for the development of the numerical code PGCtherm3D and three anonymous reviewers for useful comments, which helped to improve the manuscript. This work was partially funded by the U.S. National Science Foundation through Grant EAR-1620604 to I.W and the University of Minnesota in the form of start-up funds. The data files containing the modeling results can be obtained by contacting the author iwada@umn.edu.

References

Abers, Geoffrey A., van Keken, P.E., Kneller, E.A., Ferris, A., Stachnik, J.C., 2006. The thermal structure of subduction zones constrained by seismic imaging: implications for slab dehydration and wedge flow. Earth Planet. Sci. Lett. 241 (3–4), 387–397. https://doi.org/10.1016/j.epsl.2005.11.055.

Abers, G.A., Van Keken, P.E., Hacker, B.R., 2017. The cold and relatively dry nature of mantle forearcs in subduction zones. Nat. Geosci. 10 (5), 333–337. https://doi.org/ 10.1038/ngeo2922.

Alisic, L., Gurnis, M., Stadler, G., Burstedde, C., Ghattas, O., 2012. Multi-scale dynamics and rheology of mantle flow with plates. J. Geophys. Res. Solid Earth 117 (10), 1–27. https://doi.org/10.1029/2012JB009234.

- Antonijevic, S., Wagner, L.S., Beck, S.L., Long, M.D., Zandt, G., Tavera, H., 2016. Effects of change in slab geometry on the mantle flow and slab fabric in Southern Peru. J. Geophys. Res. Solid Earth 121, 7252–7270. https://doi.org/10.1002/2016.JB013064
- Arcay, D., Tric, E., Doin, M.P., 2005. Numerical simulations of subduction zones. Effect of slab deghydration on the mantle wedge dynamics. Physics of the Earth and Planetary Interiors 149, 133–153. https://doi.org/10.1016/j.pepi.2004.08.020.
- Bengtson, A.K., van Keken, P.E., 2012. Three-dimensional thermal structure of subduction zones: effects of obliquity and curvature. Solid Earth 3 (2), 365–373. https://doi.org/10.5194/se-3-365-2012.
- Cerpa, N.G., Wada, I., Wilson, C.R., 2017. Fluid migration in the mantle wedge: Influence of mineral grain size and mantle compaction. Journal of Geophysical Research: Solid Earth 122(8, 6247–6268. https://doi.org/10.1002/2017JB014046.
- Conrad, C.P., Behn, M.D., Silver, P.G., 2007. Global mantle flow and the development of seismic anisotropy: differences between the oceanic and continental upper mantle. J. Geophys. Res. Solid Earth 112 (7), 1–17. https://doi.org/10.1029/2006JB004608.
- Currie, Claire A., Hyndman, R.D., 2006. The thermal structure of subduction zone back arcs. J. Geophys. Res. Solid Earth 111 (8), 1–22. https://doi.org/10.1029/
- Currie, C.A., Wang, K., Hyndman, R.D., He, J., 2004. The thermal effects of steady-state slab-driven mantle flow above a subducting plate: the Cascadia subduction zone and backarc. Earth Planet. Sci. Lett. 223 (1–2), 35–48. https://doi.org/10.1016/j. epsl. 2004.04.020.
- DeMets, C., Gordon, R.G., Argus, D.F., 2010. Geologically current plate motions. Geophysical Journal International 181(1, 1–80. https://doi.org/10.1111/j.1365-246X.2009.04491.x.
- Eberhart-Phillips, Donna, Reyners, M., Chadwick, M., Stuart, G., 2008. Three-dimensional attenuation structure of the Hikurangi subduction zone in the central North Island, New Zealand. Geophys. J. Int. 174 (1), 418–434. https://doi.org/10.1111/j.1365-246X.2008.03816.x.
- England, P., Engdahl, R., Thatcher, W., 2004. Systematic variation in the depths of slabs beneath arc volcanoes. Geophys. J. Int. 156 (2), 377–408. https://doi.org/10.1111/ j.1365-246X.2003.02132.x.
- Faccenda, M., Capitanio, F.A., 2012. Development of mantle seismic anisotropy during subduction-induced 3-D flow. Geophys. Res. Lett. 39 (11), 1–5. https://doi.org/ 10.1029/2012GL051988.
- Faccenda, M., Capitanio, F.A., 2013. Seismic anisotropy around subduction zones: insights from three-dimensional modeling of upper mantle deformation and SKS splitting calculations. Geochem. Geophys. Geosystems 14 (1), 243–262. https://doi. org/10.1002/ggge.20055.
- Funiciello, F., Moroni, M., Piromallo, C., Faccenna, C., Cenedese, A., Bui, H.A., 2006. Mapping mantle flow during retreating subduction: laboratory models analyzed by feature tracking. J. Geophys. Res. Solid Earth 111 (3), 1–16. https://doi.org/10.1029/2005.1B003792.
- Furukawa, Y., 1993. Depth of the decoupling plate interface and thermal structure under arcs. J. Geophys. Res. 98 (B11), 20005–20013. https://doi.org/10.1029/ 03.IB02020
- Gaetani, G.A., Grove, T.L., 1998. The influence of water on melting of mantle peridotite. Contrib. Mineral. Petrol. 131 (4), 323–346. https://doi.org/10.1007/ s004100050396.
- Gerya, T.V., Meilick, F.I., 2011. Geodynamic regimes of subduction under an active margin: effects of rheological weakening by fluids and melts. J. Metamorph. Geol. 29 (1), 7–31. https://doi.org/10.1111/j.1525-1314.2010.00904.x.
- Gerya, Taras V., Yuen, D.A., 2003. Rayleigh Taylor instabilities from hydration and melting propel "cold plumes" at subduction zones. Earth Planet. Sci. Lett. 212 (1–2), 47–62. https://doi.org/10.1016/S0012-821X(03)00265-6.
- Grove, T.L., Chatterjee, N., Parman, S.W., Médard, E., 2006. The influence of H2O on mantle wedge melting. Earth Planet. Sci. Lett. 249 (1–2), 74–89. https://doi.org/ 10.1016/j.epsl.2006.06.043.
- Hacker, B.R., Peacock, S.M., Abers, G.A., Holloway, S.D., 2003. Subduction factory 2. Are intermediate-depth earthquakes in subducting slabs linked to metamorphic dehydration reactions? J. Geophys. Res. Solid Earth 108 (B1). https://doi.org/ 10.1029/2001JB001129.
- Hayes, G.P., Moore, G.L., Portner, D.E., Hearne, M., Flamme, H., Furtney, M., Smoczyk, G.M., 2018. Zone Geometry Model 61 (October), 58–61.
- Hebert, L.B., Antoshechkina, P., Asimow, P., Gurnis, M., 2009. Emergence of a low-viscosity channel in subduction zones through the coupling of mantle flow and thermodynamics. Earth and Planetary Science Letters 278(3–4, 243–256. https://doi.org/10.1016/j.epsl.2008.12.013.
- Hilairet, N., Reynard, B., Wang, Y., Daniel, I., Merkel, S., Nishiyama, N., Petitgirard, S., 2007. High-pressure creep of serpentine, interseismic deformation, and initiation of subduction. Science 318 (5858), 1910–1913. https://doi.org/10.1126/ science.1148494.
- Hirauchi, K.I., den Hartog, S.A.M., Spiers, C.J., 2013. Weakening of the slab-mantle wedge interface induced by metasomatic growth of talc. Geology 41 (1), 75–78. https://doi.org/10.1130/G33552.1.
- Hirth, G., Kohlstedt, D., 2003. Rheology of the upper mantle and the mantle wedge: a view from the experimentalists, in inside the subduction factory. In: Eiler, J. (Ed.), Geophys. Monogr. Ser, vol. 138. AGU, Washington, D.C, pp. 83–105.
- Hoernle, K., Abt, D.L., Fischer, K.M., Nichols, H., Hauff, F., Abers, G.A., et al., 2008. Arc-parallel flow in the mantle wedge beneath Costa Rica and Nicaragua. Nature 451 (7182, 1094–1097. https://doi.org/10.1038/nature06550.
- Holtzman, B.K., Kohlstedt, D.L., Zimmerman, M.E., Heidelbach, F., Hiraga, T., Hustoft, J., 2003. Melt segregation and strain partitioning: Implications for seismic anisotropy and mantle flow. Science 301(5637, 1227–1230. https://doi.org/ 10.1126/science.1087132.

- Honda, S., 1985. Thermal structure beneath Tohoku, northeast Japan-a case study for understanding the detailed thermal structure of the subduction zone. Tectonophysics 112, 69–102. https://doi.org/10.1017/CBO9781107415324.004.
- Honda, S., Yoshida, T., 2005. Effects of oblique subduction on the 3-D pattern of small-scale convection within the mantle wedge. Geophys. Res. Lett. 32 (13), 1–4. https://doi.org/10.1029/2005GL023106.
- Honda, S., Gerya, T., Zhu, G., 2010. A simple three-dimensional model of thermochemical convection in the mantle wedge. Earth Planet. Sci. Lett. 290 (3–4), 311–318. https://doi.org/10.1016/j.epsl.2009.12.027.
- Ishise, M., Kawakatsu, H., Morishige, M., Shiomi, K., 2018. Radial and Azimuthal Anisotropy Tomography of the NE Japan Subduction Zone: Implications for the Pacific Slab and Mantle Wedge Dynamics. Geophysical Research Letters 45(9, 3923–3931. https://doi.org/10.1029/2018GL077436.
- Jadamec, Margarete A., Billen, M.I., 2010. Reconciling surface plate motions with rapid three-dimensional mantle flow around a slab edge. Nature 465 (7296), 338–341. https://doi.org/10.1038/nature09053.
- Jadamec, M.A., Billen, M.I., 2012. The role of rheology and slab shape on rapid mantle flow: three-dimensional numerical models of the Alaska slab edge. J. Geophys. Res. Solid Earth 117 (2), 1–20. https://doi.org/10.1029/2011JB008563.
- Ji, Y., Yoshioka, S., 2015. Effects of slab geometry and obliquity on the interplate thermal regime associated with the subduction of three-dimensionally curved oceanic plates. Geosci. Front. 6 (1), 61–78. https://doi.org/10.1016/j.gsf.2014.04.011.
- Jung, H., Karato, S.I., 2001. Water-induced fabric transitions in olivine. Science 293 (5534), 1460–1463. https://doi.org/10.1126/science.1062235.
- Karato, S., Jung, H., Katayama, I., Skemer, P., 2008. Geodynamic significance of seismic anisotropy of the upper mantle: New insights from laboratory studies. Annual Review of Earth and Planetary Sciences 36, 59–95.
- Katayama, I., Karato, Sichiro, 2006. Effect of temperature on the B- to C-type olivine fabric transition and implication for flow pattern in subduction zones. Phys. Earth Planet. Inter. 157 (1–2), 33–45. https://doi.org/10.1016/j.pepi.2006.03.005.
- Katayama, I., Hirauchi, K.I., Michibayashi, K., Ando, J.I., 2009. Trench-parallel anisotropy produced by serpentine deformation in the hydrated mantle wedge. Nature 461 (7267), 1114–1117. https://doi.org/10.1038/nature08513.
- Király, Á., Capitanio, F.A., Funiciello, F., Faccenna, C., 2017. Subduction induced mantle flow: length-scales and orientation of the toroidal cell. Earth Planet. Sci. Lett. 479, 284–297. https://doi.org/10.1016/j.epsl.2017.09.017.
- Kneller, E.A., van Keken, P.E., 2008. Effect of three-dimensional slab geometry on deformation in the mantle wedge: implications for shear wave anisotropy. Geochem. Geophys. Geosystems 9 (1), 1–21. https://doi.org/10.1029/2007GC001677.
- Kneller, E.A., van Keken, P.E., Karato, S.I., Park, J., 2005. B-type olivine fabric in the mantle wedge: insights from high-resolution non-Newtonian subduction zone models. Earth Planet. Sci. Lett. 237 (3–4), 781–797. https://doi.org/10.1016/j. epsl. 2005.06.049.
- Kneller, E.A., Long, M.D., van Keken, P.E., 2008. Olivine fabric transitions and shear wave anisotropy in the Ryukyu subduction system. Earth Planet. Sci. Lett. 268 (3–4), 268–282. https://doi.org/10.1016/j.epsl.2008.01.004.
- Lee, C., Wada, I., 2017. Clustering of arc volcanoes caused by temperature perturbations in the back-arc mantle. Nat. Commun. 8 (May 2016), 1–9. https://doi.org/10.1038/ncomms15753
- Lee, C., Wada, I., 2021. Volcano clustering promoted by the cessation of back-arc spreading and ensuing nascent lithospheric drips. Geophys. Res. Lett. https://doi. org/10.1029/2020GL091433.
- Long, M.D., Becker, T.W., 2010. Mantle dynamics and seismic anisotropy. Earth Planet. Sci. Lett. 297 (3–4), 341–354. https://doi.org/10.1016/j.epsl.2010.06.036.
- Long, M.D., Silver, P.G., 2008. The subduction zone flow field from seismic anisotropy: a global view. Science 319 (5861), 315–318. https://doi.org/10.1126/ science.1150809.
- Long, M.D., Wirth, E.A., 2013. Mantle flow in subduction systems: the mantle wedge flow field and implications for wedge processes. J. Geophys. Res. Solid Earth 118 (2), 583–606. https://doi.org/10.1002/jgrb.50063.
- Manea, V.C., Manea, M., Ferrari, L., Orozco, T., Valenzuela, R.W., Husker, A., Kostoglodov, V., 2017. A review of the geodynamic evolution of flat slab subduction in Mexico, Peru, and Chile. Tectonophysics 695 (January), 27–52. https://doi.org/ 10.1016/j.tecto.2016.11.037.
- Menant, A., Sternai, P., Jolivet, L., Guillou-Frottier, L., Gerya, T., 2016. 3D numerical modeling of mantle flow, crustal dynamics and magma genesis associated with slab roll-back and tearing: the eastern Mediterranean case. Earth Planet. Sci. Lett. 442, 93–107. https://doi.org/10.1016/j.epsl.2016.03.002.
- Morishige, M., van Keken, P.E., 2014. Along-arc variation in the 3-D thermal structure around thejunction between the Japan and Kurile arcs. Geochem. Geophys. Geosystems 2225–2240. https://doi.org/10.1002/2014GC005394.Received.
- Morra, G., Regenauer-Lieb, K., Giardini, D., 2006. Curvature of oceanic arcs. Geology 34 (10), 877–880. https://doi.org/10.1130/G22462.1.
- Nakajima, J., Shimizu, J., Hori, S., Hasegawa, A., 2006. Shear-wave splitting beneath the southwestern Kurile arc and northeastern Japan arc: a new insight into mantle return flow. Geophys. Res. Lett. 33 (5), 1–4. https://doi.org/10.1029/2005GL025053.
- Philippon, M., Corti, G., 2016. Obliquity along plate boundaries. Tectonophysics 693, 171–182. https://doi.org/10.1016/j.tecto.2016.05.033.
- Plunder, A., Thieulot, C., Van Hinsbergen, D.J.J., 2018. The effect of obliquity on temperature in subduction zones: insights from 3-D numerical modeling. Solid Earth 9 (3), 759–776. https://doi.org/10.5194/se-9-759-2018.
- Ramos, V.A., Folguera, A., 2009. Andean flat-slab subduction through time. Geol. Soc. Spec. Publ. 327, 31–54. https://doi.org/10.1144/SP327.3.
- Rosas, J.C., Currie, C.A., He, J., 2016. Three-dimensional thermal model of the Costa Rica-Nicaragua Subduction Zone. Pure Appl. Geophys. 173 (10–11), 3317–3339. https://doi.org/10.1007/s00024-015-1197-4.

- Rychert, C.A., Fischer, K.M., Abers, G.A., Plank, T., Syracuse, E., Protti, J.M., et al., 2008. Strong along-arc variations in attenuation in the mantle wedge beneath Costa Rica and Nicaragua. Geochem. Geophys. Geosystems 9 (10). https://doi.org/10.1029/ 2008GC002040
- Schellart, W.P., 2017. Andean mountain building and magmatic arc migration driven by subduction-induced whole mantle flow. Nat. Commun. 8 (1) https://doi.org/ 10.1038/s41467-017-01847-z.
- Skemer, P., Hansen, L.N., 2016. Inferring upper-mantle flow from seismic anisotropy: an experimental perspective. Tectonophysics 668–669, 1–14. https://doi.org/10.1016/ j.tecto.2015.12.003.
- Stachnik, J.C., Abers, G.A., Christensen, D.H., 2004. Seismic attenuation and mantle wedge temperatures in the Alaska subduction zone. J. Geophys. Res. Solid Earth 109 (10), 1–17. https://doi.org/10.1029/2004JB003018.
- Stadler, G., Gurnis, M., Burstedde, C., Wilcox, L.C., Alisic, L., Ghattas, O., 2010. The dynamics of plate tectonics and mantle flow: From local to global scales. Science 329, 1033–1038. https://doi.org/10.1126/science.1191223.
- Stegman, D.R., Farrington, R., Capitanio, F.A., Schellart, W.P., 2010. A regime diagram for subduction styles from 3-D numerical models of free subduction. Tectonophysics 483 (1–2), 29–45. https://doi.org/10.1016/j.tecto.2009.08.041.
- Stein, C.A., Stein, S., 1992. A model for the global variation in oceanic depth and heat flow with litho. Nature 359, 710–713.
- Strak, V., Schellart, W.P., 2014. Evolution of 3-D subduction-induced mantle flow around lateral slab edges in analogue models of free subduction analysed by stereoscopic particle image velocimetry technique. Earth Planet. Sci. Lett. 403, 368–379. https:// doi.org/10.1016/j.epsl.2014.07.007.
- Syracuse, E.M., Abers, G.A., 2006. Global compilation of variations in slab depth beneath arc volcanoes and implications. Geochem. Geophys. Geosystems 7 (5). https://doi. org/10.1029/2005GC001045.

- Syracuse, E.M., van Keken, P.E., Abers, G.A., Suetsugu, D., Bina, C., Inoue, T., et al., 2010. The global range of subduction zone thermal models. Phys. Earth Planet. Inter. 183 (1–2), 73–90. https://doi.org/10.1016/j.pepi.2010.02.004.
- Till, C.B., Grove, T.L., Withers, A.C., 2012. The beginnings of hydrous mantle wedge melting. Contrib. Mineral. Petrol. 163 (4), 669–688. https://doi.org/10.1007/ s00410-011-0692-6.
- Uchida, N., Nakajima, J., Wang, K., Takagi, R., Yoshida, K., Nakayama, T., et al., 2020. Stagnant forearc mantle wedge inferred from mapping of shear-wave anisotropy using S-net seafloor seismometers. Nat. Commun. 11 (1) https://doi.org/10.1038/s41467-020-19541-y.
- van Keken, P.E., Hacker, B.R., Syracuse, E.M., Abers, G.A., 2011. Subduction factory: 4. Depth-dependent flux of H2O from subducting slabs worldwide. Journal of Geophysical Research: Solid Earth 116(1. https://doi.org/10.1029/2010JB007922.
- Wada, I., Wang, K., 2009. Common depth of slab-mantle decoupling: reconciling diversity and uniformity of subduction zones. Geochem. Geophys. Geosystems 10 (10). https://doi.org/10.1029/2009GC002570.
- Wada, I., He, J., Hasegawa, A., Nakajima, J., 2015. Mantle wedge flow pattern and thermal structure in Northeast Japan: effects of oblique subduction and 3-D slab geometry. Earth Planet. Sci. Lett. 426. https://doi.org/10.1016/j.epsl.2015.06.021.
- Wagner, L.S., Jaramillo, J.S., Ramírez-Hoyos, L.F., Monsalve, G., Cardona, A., Becker, T. W., 2017. Transient slab flattening beneath Colombia. Geophys. Res. Lett. 44 (13), 6616–6623. https://doi.org/10.1002/2017GL073981.
- Wilson, C.R., Spiegelman, M., van Keken, P.E., Hacker, B.R., 2014. Fluid flow in subduction zones: the role of solid rheology and compaction pressure. Earth Planet. Sci. Lett. 401, 261–274. https://doi.org/10.1016/j.epsl.2014.05.052.